Magnetic behavior of $Ba_3Cu_3Sc_4O_{12}$

2012 J. Phys.: Condens. Matter 24 236001

(http://iopscience.iop.org/0953-8984/24/23/236001)

J. Phys.: Condens. Matter **24** (2012) 236001 (13pp) doi:10.1088/0953-8984/24/23/236001

Magnetic behavior of $Ba_3Cu_3Sc_4O_{12}$

B Koteswararao[1], A V Mahajan[1], F Bert[2], P Mendels[2], J Chakraborty[3], V Singh[1,3], I Dasgupta[1,3], S Rayaprol[4], V Siruguri[4], A Hoser[5] and S D Kaushik[4]

[1] Department of Physics, Indian Institute of Technology Bombay, Mumbai 400076, India
[2] Laboratoire de Physique des Solides, Université Paris-Sud, UMR8502, CNRS, 91405 Orsay Cedex, France
[3] Department of Solid State Physics, Indian Association for the Cultivation of Science, Jadavpur, Kolkata 700 032, India
[4] UGC-DAE Consortium for Scientific Research, Mumbai Centre, R-5 Shed, Bhabha Atomic Research Centre, Mumbai 400 085, India
[5] Helmholtz-Zentrum Berlin für Materialien und Energie GmbH, Hahn-Meitner-Platz 1, D-14109 Berlin, Germany

E-mail: mahajan@phy.iitb.ac.in

Received 2 March 2012, in final form 16 April 2012
Published 9 May 2012
Online at stacks.iop.org/JPhysCM/24/236001

Abstract
The chain-like system $Ba_3Cu_3Sc_4O_{12}$ has potentially interesting magnetic properties due to the presence of Cu^{2+} and a structure-suggested low dimensionality. We present magnetization M versus magnetic field H and temperature T, T- and H-dependent heat-capacity C_p, ^{45}Sc nuclear magnetic resonance (NMR), muon spin rotation (μSR), neutron diffraction measurements and electronic structure calculations for $Ba_3Cu_3Sc_4O_{12}$. The onset of magnetic long-range antiferromagnetic (AF) order at $T_N \sim 16$ K is consistently evidenced from the whole gamut of our data. A significant sensitivity of T_N to the applied magnetic field H ($T_N \sim 0$ K for $H = 70$ kOe) is also reported. Coupled with a ferromagnetic Curie–Weiss temperature ($\theta_{CW} \sim 65$ K) in the susceptibility (from a 100 to 300 K fit), it is indicative of competing ferromagnetic and antiferromagnetic interactions. These indications are corroborated by our density functional theory based electronic structure calculations, where we find the presence of significant ferromagnetic couplings between some copper ions whereas AF couplings were present between some others. Our experimental data, backed by our theoretical calculations, rule out the one-dimensional magnetic behavior suggested by the structure and the observed long-range order is due to the presence of non-negligible magnetic interactions between adjacent as well as next-nearest chains.

(Some figures may appear in colour only in the online journal)

1. Introduction

One-dimensional magnetic systems are recognized as an ideal playground in the search for novel states of matter. Indeed, by varying the interactions (near neighbor, next-nearest neighbor) various states can be stabilized and have been the focus of experimental studies in the recent past, where high-field magnetization experiments have played a central role. Their experimental exploration has in turn induced some theoretical developments to understand the observed properties. Various models for one-dimensional magnetic systems with different spin Hamiltonians have been theoretically investigated. It is only in the past 10–15 years that experimentalists have come up with actual realizations of different model systems. Clearly, real systems are quite often much more complex compared to simple models. In such cases, further efforts by theorists, based on information pertaining to a real system, often lead to an improved understanding of its properties. Among the various chain-like $S = \frac{1}{2}$ antiferromagnetic (AF) systems investigated, a compound with a 'diamond-chain' geometry has been under focus recently. The system consists of isolated chains of corner-shared diamonds (squares). With the presence of antiferromagnetic couplings and the possibility of frustrated nearest-neighbor interactions (due to the two edge-shared triangles within a diamond), exotic physics might

result. In practice, $Cu_3(CO_3)_2(OH)_2$ or azurite is the only compound investigated with the diamond-chain structure. Measurements of the susceptibility, heat capacity, and high-field magnetization in this compound have revealed it to be a prototypical substance for the frustrated diamond-chain model [1]. High-field magnetization data evidence the presence of a 1/3 magnetization plateau. If one considers the chain to comprise of alternating dimers and monomers, this plateau is thought to arise due to complete polarization of the monomers by the applied magnetic field. As for the correct model which could describe the experimental data, the initial work suggested all the interactions to be antiferromagnetic. However, inelastic neutron scattering experiments [2] actually suggested that one of the interactions between the spins comprising the dimer and the monomer was ferromagnetic. In contrast, later numerical studies [3] found that all the experimental data could be explained by considering a model where all the interactions were antiferromagnetic (and therefore strongly frustrated) and there also existed an interaction between the monomers. Motivated by this work, we thought it would be interesting to search for other systems with a similar geometry, the studies on which might help to elucidate the physics behind the unusual features of azurite. One such possible system could be $Ba_3Cu_3Sc_4O_{12}$ (BCSO).

At first sight, the structure of BCSO is quite appealing. Consider the CuO_4 plaquette as a unit. Now imagine a square made up of four such units with Cu at the vertices. If we arrange these squares in a corner-sharing configuration, we will get the classic diamond-chain. In BCSO, the only difference with respect to the classic diamond-chain is that the adjacent squares have their planes orthogonal to each other (rotated about the diagonal). Given that there has been hardly any experimental/theoretical work pertaining to BCSO except for structural studies [4] and a nuclear magnetic resonance (NMR) investigation [5], BCSO therefore appears to be a fit case for further investigation. There are two important issues that need to be addressed. (i) Are the magnetic linkages as simple as suggested by the structure? The magnetism would therefore be that of a low-dimensional compound. (ii) What are the dominant magnetic interactions and what are their relative magnitudes and signs?

With the above considerations in mind we have undertaken a detailed investigation of BCSO. Bulk techniques such as susceptibility, heat capacity and neutron diffraction have been used to establish the gross nature of magnetism in the material. Local probe ^{45}Sc NMR has helped us to determine the local magnetic and structural properties via a measurement of the ^{45}Sc NMR shift and the line shape. The main outcome of the above measurements is that BCSO does not show any signs of low dimensionality in the temperature range investigated (1.8–300 K). On the contrary, clear evidence of AF order at $T_N = 16$ K from the bulk (∼100%, as shown from zero field μSR) of the sample, is seen while susceptibility data at high-T (100–300 K) are indicative of ferromagnetic interactions. One of the goals of the present paper is to reconcile this apparent contrast between the expectations based on atomic arrangements and the observed LRO, and to provide a basis for understanding ferromagnetic interactions at high-T but AF order at low-T. In order to address these issues, we have carried out electronic structure calculations based on density functional theory. We have also calculated various exchange interactions in the Generalized Gradient Approximation GGA + U framework (here, U is the on-site Coulomb repulsion energy). The results of these calculations enable us to resolve the apparent surprises of the experimental data. The main conclusion is that the strongest magnetic interaction in BCSO is between a Cu and its nearest neighbor and is ferromagnetic. The diagonal interactions (in the diamond) and also the next-nearest-neighbor interactions along the chain are AF and substantial (about half the magnitude of the nearest-neighbor couplings). The observed LRO appears to be due to comparably strong couplings between neighboring chains. Due to the frustration generated by a mixture of comparable F and AF couplings, the system is susceptible to the loss of LRO in moderate applied magnetic fields.

The paper is organized as follows. Following the section on experimental details, we present the results of our various measurements corresponding to the paramagnetic state of BCSO. While the x-ray diffraction and neutron diffraction data validate the structure of BCSO, bulk susceptibility and heat capacity help characterize the magnetic interactions and the lattice properties. We next discuss results which establish the onset of LRO in BCSO at $T \sim 16$ K. This is followed by presentation of the results for the T-region below the ordering temperature, including the effect of an applied magnetic field on the ordering temperature. This is followed by a discussion section that uses the results of our electronic structure calculations, which are instrumental in obtaining a coherent understanding of the experimental data. The important conclusions are given in section 4.

2. Experimental details

The polycrystalline samples of $Ba_3Cu_3Sc_4O_{12}$ were synthesized by a solid state reaction route with stoichiometric amounts of $BaCO_3$ (99.99%), CuO (99.7%), and Sc_2O_3 (99.99%). These amounts were ground, pelletized, and fired in a alumina crucible at 850–1050 °C in air for 4 days, with regrinding every 24 h. Samples were quench-cooled to room temperature in air. Powder x-ray diffraction data were collected using a PANalytical *X*'pert PRO powder diffractometer with Cu Kα radiation. The Rietveld refinements were carried out using Fullprof software [6], and confirmed the single-phase nature of the sample. Magnetization (M) measurements were done in the temperature (T) range from 2 to 300 K and in the magnetic field (H) range 0–90 kOe using a SQUID magnetometer (MPMS) and a vibrating sample magnetometer VSM (PPMS), both from Quantum Design. Heat capacity measurements as a function of T and H were also performed using the PPMS by the thermal relaxation method. Further, we have carried out ^{45}Sc NMR spectra measurements in the temperature range from 1.2 to 80 K using a spectrometer fitted with a magnet having a sweepable field. This was done at various fixed frequencies. The spectra were measured from 80 to 300 K

using the spectrometer with a fixed field of about 70 kOe. The preparation and bulk measurements were done at IIT Bombay while the NMR work was done at the Laboratoire de Physique des Solides (LPS), Orsay. The μSR measurements were performed to probe the ordering at Paul Scherrer Institut (PSI), Villigen (Switzerland). Neutron diffraction (ND) measurements were carried out on powder samples using a focusing crystal diffractometer (FCD) set up by the UGC-DAE Consortium for Scientific Research Mumbai Centre at the Dhruva reactor, Mumbai (India) at a wavelength of 1.48 Å [7] and the diffractometer E6 installed at the BERII reactor (Helmholtz-Zentrum Berlin) at a wavelength of 2.45 Å. For both experiments, the powder sample was filled in a vanadium can. ND experiments were carried out in the temperature range 2–300 K and also under external magnetic fields up to 80 kOe. For in-field experiments, a mixture of deuterated methanol and ethanol was used as a binder to avoid a preferred orientation of samples due to the magnetic field. ND patterns were analyzed by the Rietveld method using the program FullProf for the refinement of chemical and magnetic structures. The results of our measurements and calculations will be described in the following sections.

3. Experimental results and analysis

$Ba_3Cu_3Sc_4O_{12}$ crystallizes with a tetragonal structure in the space group $I4/mcm$ (No. 140). The lattice parameters obtained by us are $a = 11.9021$ Å, $c = 8.3962$ Å, $z = 4$, and $c/a = 0.71$, which are in good agreement with previously reported values [4].

The structure of $Ba_3Cu_3Sc_4O_{12}$ was first reported by Gregory [4]. The crystal structure is shown in figure 1. In this figure, the chain formed by Cu and O atoms (enclosed by blue dashed lines with an arrow mark) is shown separately. The chains consist of diamond-(or square-)like units, which are built from two types of CuO_4 units ($Cu(1)O_4$ and $Cu(2)O_4$), as shown in figure 1. The Cu atoms in the square are coupled to their nearest neighbors via an oxygen with a Cu–O–Cu bond angle of ∼90°. Successive Cu-squares (formed by four Cu atoms) are corner shared with their planes perpendicular to each other. The chains are separated by Ba atoms. Looking at these figures, one can get the impression that there exist diamond-like chains in the c-direction.

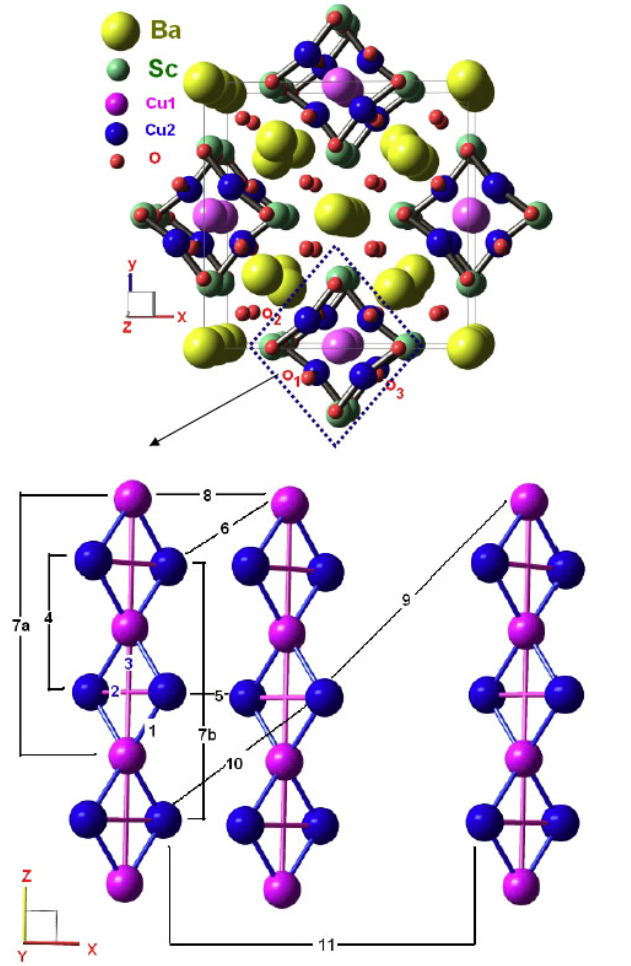

Figure 1. The crystal structure of $Ba_3Cu_3Sc_4O_{12}$. The diamond-like chains formed, by Cu1 and Cu2 atoms, travel along the c-direction. The notation for the various hopping integrals is also indicated.

3.1. Probing the paramagnetic state and the ordering using bulk probes

3.1.1. Magnetization. In figure 2(a), $\chi(T) = M/H$ increases with decreasing T in a Curie–Weiss manner. Although the structure is suggestive of a one-dimensional spin system, no broad maximum was seen in $\chi(T)$. The inverse of $\chi(T)$ versus T is also plotted in the right y-axis of figure 2(a). The high temperature (200–300 K) $\chi(T)$ is described well by the Curie–Weiss law $\chi(T) = \chi_0 + C/(T - \theta_{CW})$, with $\chi_0 = -(7 \pm 1) \times 10^{-5}$ cm^3 mol^{-1} Cu, $C = 0.413$ cm^3 K mol^{-1} Cu (fixed to this value corresponding to $S = \frac{1}{2}$ and $g = 2.1$), and $\theta_{CW} = 65 \pm 2$ K. The positive value of Curie–Weiss temperature, $\theta_{CW} = 65 \pm 2$ K, suggests that the major exchange couplings are ferromagnetic at high temperature. Here χ_0 is the sum of the diamagnetic susceptibility χ_{core} and Van Vleck susceptibility χ_{vv}. The core diamagnetic susceptibility is calculated to be about -9.63×10^{-5} cm^3 mol^{-1} Cu [8]. This yields $\chi_{vv} \sim (2.6 \pm 1.0) \times 10^{-5}$ cm^3 mol^{-1} Cu, which is comparable with other cuprates. The sharp maximum in the susceptibility at about 16 K indicates AF LRO in this system. The ratio θ_{CW}/T_N∼4 admits the possibility of a moderate level of frustration in our system. The presence of ferromagnetic interactions at high temperature and antiferromagnetic ordering at low temperature in this sample is interesting enough to motivate further measurements.

To understand the nature of ordering in the sample, we have measured $\chi(T)$ in various H of 100 Oe, 20, 30, 40, 60, and 80 kOe in the T-range 2–50 K, as shown in figure 2(b). There is no difference found in the data of zero field cooling (ZFC) and field cooling (FC) $\chi(T)$ measured at 100 Oe. This indicates that the system does not have disordered or spin-glass-like behavior. The T_N decreases with H, which is also a clear indication that the ordering is of the antiferromagnetic kind. Surprisingly, T_N vanishes even

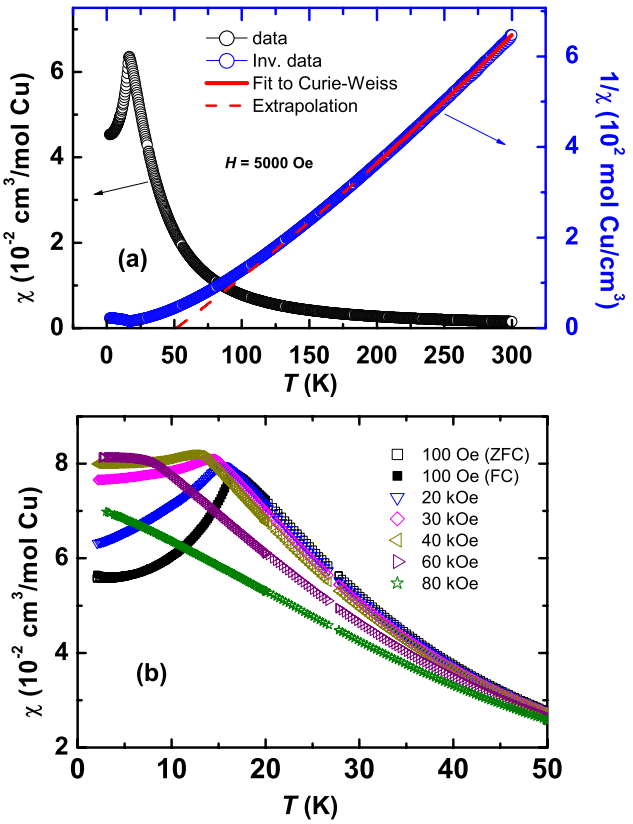

Figure 2. (a) The T-dependence of magnetic susceptibility (left y-axis) and inverse susceptibility (right y-axis) of $Ba_3Cu_3Sc_4O_{12}$ are plotted. (b) $\chi(T)$ in various applied fields. The ordering is seen to be suppressed by the applied fields.

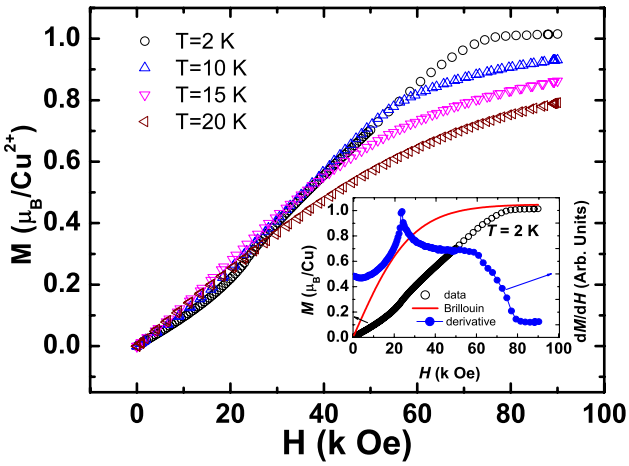

Figure 3. Magnetization as a function of the applied field $M(H)$ measured at various temperatures from 2 to 20 K. Inset shows the plot of $M(H)$ at 2 K on the left y-axis. The derivative of the magnetization is plotted on the right y-axis. The solid line is the generated Brillouin function for $S = \frac{1}{2}$ and $g = 2.1$ at $T = 2$ K.

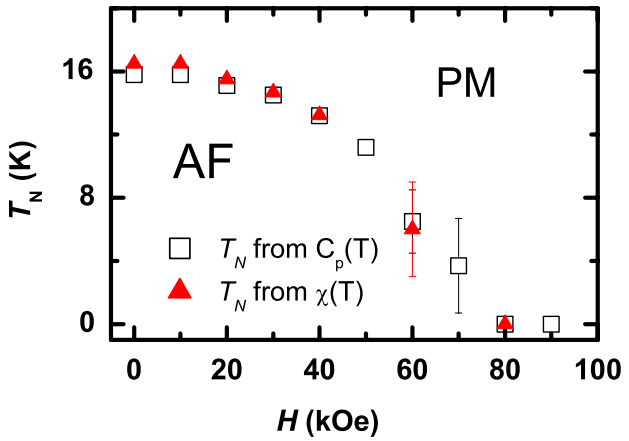

Figure 4. The variation of T_N with applied fields. The data points in the plot separate the antiferromagnetic (AF) and paramagnetic (PM) regions.

at a relatively small field at about 60–80 kOe. In a field of 60 kOe, the sharp peak in $\chi(T)$ disappears and $\chi(T)$ is nearly independent of temperature. The value of $\chi(T)$ at 80 kOe does not have any anomaly. Magnetization M data as a function of H up to 90 kOe at different Ts are shown in figure 3. The obtained T_Ns from $\chi(T)$ are plotted in figure 4. In the case of $M(H)$ at 2 K, M increases with field and saturates to about 1 μ_B above 80 kOe, as shown in the inset of figure 3. The data are also compared with magnetization as a function of applied field at $T = 2$ K generated using the Brillouin function for isolated $S = \frac{1}{2}$ moments with $g = 2.1$ (typical for cuprates). The data at low fields have values which are smaller than the free spin behavior due to antiferromagnetic coupling between the spins at $T = 2$ K. At high fields above 80 kOe, the data follow the $S = \frac{1}{2}$ ($g = 2.1$) Brillouin function. A small change in the slope of the magnetization is observed at 2 K at $H = 23$ kOe. The change can be clearly seen in the derivative of magnetization with field. This probably arises from a spin-flop transition.

3.1.2. Heat capacity. In order to understand the field sensitive ordering in this system, we performed heat capacity measurements in different fields up to 90 kOe using the heat capacity setup (attached to the PPMS) by the thermal relaxation method. Figure 5(a) shows C_p versus T. The C_p has two contributions, lattice and magnetic. In order to separate the lattice contribution, it is normally useful to make measurements on an isostructural non-magnetic analog of the given system (possibly by replacing the Cu atoms by Zn and Mg atoms). However, there is neither any report of a non-magnetic analog of BCSO nor did we succeed in preparing such a compound. We then went ahead and analyzed the lattice part of the C_p data in the 100–200 K region using the Debye model [9]. The data could not be fit with a single Debye temperature, but we were able to fit the data to the following formula in the T-range 100–200 K, which contains a linear combination of two Debye integrals.

$$C_p(T) = 9rNk_B \sum_{i=1,2} C_i \left(\frac{T}{\theta_D^i}\right)^3 \int_0^{x_D^i} \frac{x^4 e^x}{(e^x - 1)^2}\,dx. \quad (1)$$

Here r is the number of atoms per formula unit, θ_D^i is a Debye temperature and $x_D^i = \theta_D^i/T$. The obtained parameters are $C_1 = 0.61 \pm 0.05$, $\theta_D^1 = (736 \pm 10)$ K, $C_2 = 0.33 \pm$

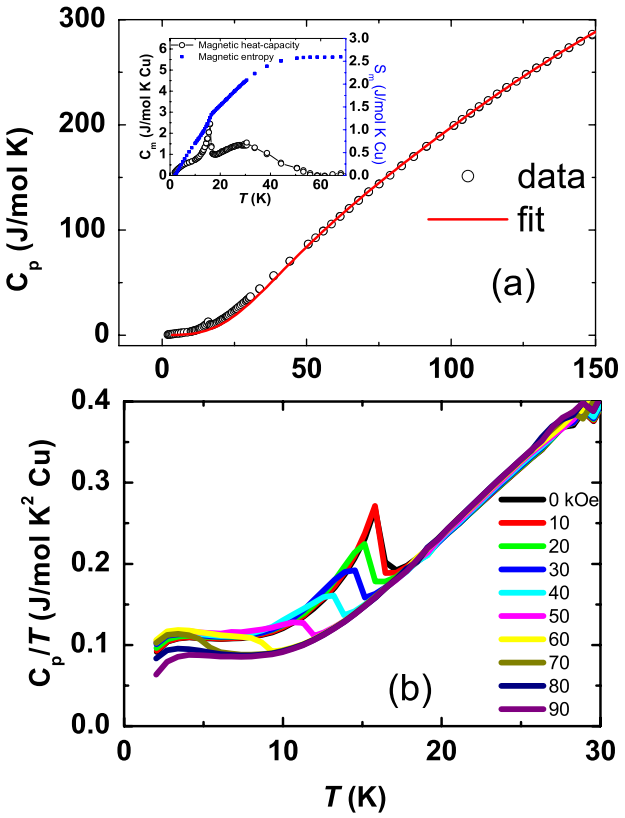

Figure 5. (a) Heat capacity versus temperature with a fit (explained in the text). Inset shows the plot of the magnetic heat capacity C_M (on left y-axis) and magnetic entropy S_M (on right y-axis) versus T (b) Variation of heat capacity divided by temperature (C_p/T) as a function of T in various applied fields from 0 to 9 T.

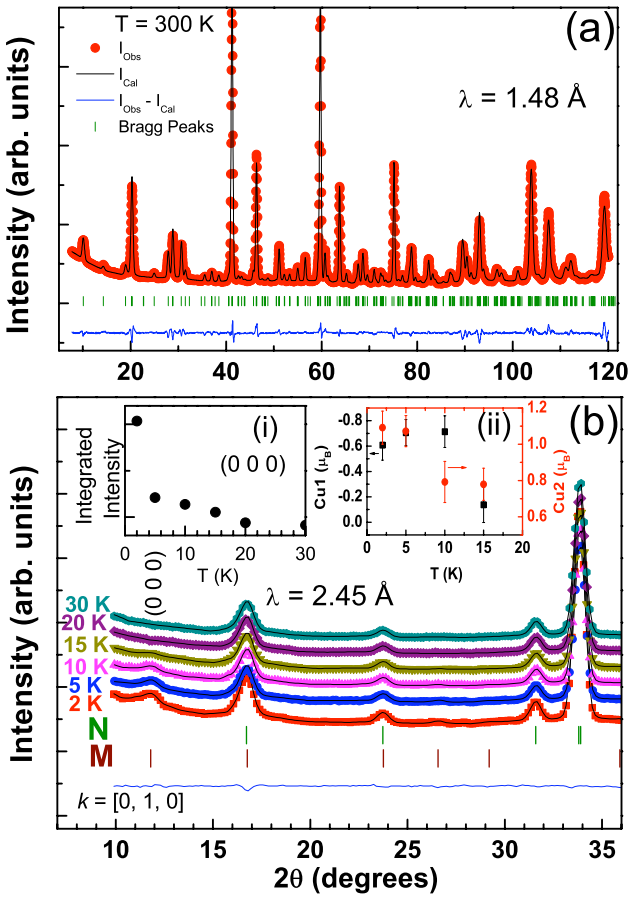

Figure 6. (a) Neutron diffraction (ND) pattern for $Ba_3Cu_3Sc_4O_{12}$ measured at $T = 300$ K refined using the Rietveld refinement method. The vertical tick marks indicate the nuclear Bragg peak positions. (b) Rietveld refined low-temperature ND patterns for $Ba_3Cu_3Sc_4O_{12}$. The magnetic peak (0 0 0) is marked for $T = 2$ K. The nuclear and magnetic Bragg peak positions are indicated by N and M respectively. Inset (i) shows the decrease in the integrated intensity of the magnetic peak with increasing temperature. Inset (ii) shows the variation of magnetic moments of Cu1 and Cu2 with temperatures.

0.05, and $\theta_D^2 = 230 \pm 30$ K. Although the fit is good, the magnetic heat capacity, obtained from C_p by subtracting the lattice contribution, has a broad maximum at about 30 K, which seems unphysical. The entropy change calculated from magnetic specific heat is about 2.6 J mol^{-1} K^{-1} Cu, which is smaller than that expected ($\sim R \ln 2$) for $S = \frac{1}{2}$ systems. Extracting the lattice contribution by fitting to a Debye model in a lower range (say 40–100 K) might help to remove the 30 K broad anomaly. However, the entropy change in that case would be even smaller. This suggests the existence of a magnetic contribution to heat capacity at temperatures much higher than T_N (the deviation from CW law in the magnetic susceptibility begins above 100 K). This is in tune with our electronic structure calculations (presented in a later section) which suggest the existence of long-range ferromagnetic couplings.

A sharp anomaly is observed at 16 K (as in $\chi(T)$), which is a clear indication of ordering. In figure 5(b), C_p/T is plotted as a function of T for various magnetic fields. The peak moves to lower temperatures as the applied field is increased, until it is smeared out and more-or-less disappears when the applied field is 80 kOe. The T_Ns (peak positions) obtained from C_p/T versus T data are in agreement with those obtained from $\chi(T)$ data (see figure 4). In addition to the 16 K anomaly (in zero field) there is also a broad maximum around 3 K in the C_p/T versus T data. While this, in principle, could be due to some change in the spin-order, we did not find any evidence of this in our μSR data down to 1.5 K. Another possibility is that it is a Schottky anomaly from $S = \frac{1}{2}$ defects. However, no significant field dependence is seen for the low-T anomaly. But this could be simply because it gets masked by the large contribution from the heat capacity from the AF part. For the same reason, any Curie-like upturn in the low-T susceptibility is overwhelmed by the large susceptibility of the AF part.

3.1.3. Neutron diffraction, Figure 6(a) shows the refinement of the neutron diffraction (ND) pattern at 300 K. Cell parameters obtained by ND are in fair agreement with the XRD results. The results of the refinement are given in table 1 along with the various R-factors. Figure 6(b) shows the ND patterns as a function of temperature up to 30 K. A weak low-angle magnetic reflection at 11.8° is clearly seen at 2 K, which gradually broadens and disappears by about 20 K. The propagation vector for the refinement of the magnetic cell was identified by using the k-search program within the Fullprof suite. The result of k-search gave a commensurate propagation vector $k = (010)$. Refinement of the ND pattern

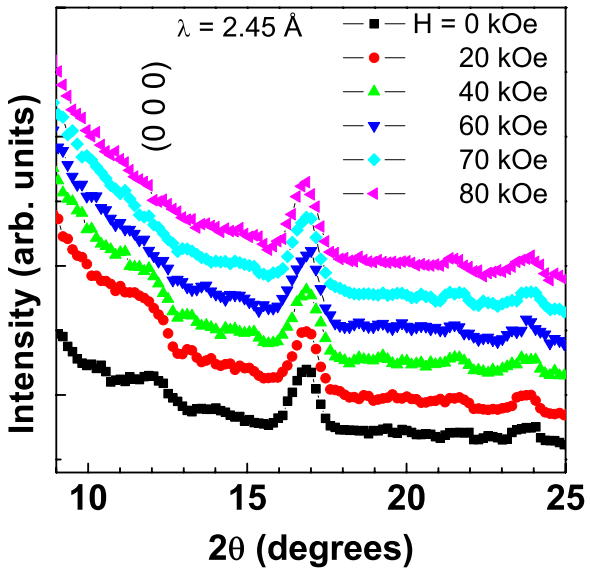

Figure 7. ND patterns for $Ba_3Cu_3Sc_4O_{12}$ measured at $T = 2$ K and various applied magnetic fields. The magnetic peak (0 0 0) broadens with increasing magnetic field.

at 2 K was done by including a magnetic phase and the propagation vector, $k = (010)$. To determine the magnetic structure, a triclinic space group, $I\bar{1}$ was used to generate a full set of reflections with proper multiplicity. The irreducible representations of the small groups were determined using the BasIreps program within the Fullprof suite. The upper tick marks belong to the nuclear phase while the lower ones are for the magnetic phase. Inset (i) of figure 6(b) shows the integrated intensity of the (0 0 0) magnetic reflection. There is no significant change observed in the structural parameters obtained at 300 and 2 K. The moment values on Cu1 and Cu2 obtained at $T = 2$ K are about -0.65 μ_B and 1.15 μ_B, respectively. Inset (ii) of figure 6(b) shows the variation of moments of these two atoms with temperature. The ND patterns taken at 2 K under external magnetic fields up to 80 kOe are shown in figure 7. The low angle magnetic reflection (0 0 0) gets completely suppressed under fields of 60 kOe and above, indicating a suppression of magnetic ordering. Considering that only one magnetic Bragg peak was clearly observed and the associated uncertainties in determining the integrated peak intensities (in the presence of a background), we feel that the obtained magnetic moment values are in tune with those from our bulk magnetization data in high fields.

The above results then clearly suggest that the BCSO system must have significant three-dimensional magnetic interactions that lead to the observed LRO. Further, our observations indicate the presence of competing magnetic interactions/frustrations. Both these suggestions are later validated by our electronic structure calculations.

3.2. Local probe measurements of the paramagnetic state and the ordered state

While the bulk probe data provide important input concerning the physical properties of the system, local probes such as μSR and NMR enable us to obtain a deeper look at the system, often giving fine details which are not accessible otherwise.

Table 1. Structural parameters after Rietveld refinement of the neutron diffraction pattern of $Ba_3Cu_3Sc_4O_{12}$ at 300 and 2 K.

Parameters	$T = 300$ K	$T = 2$ K
Space group	*I4/mcm*	*I4/mcm*
a (Å)	11.916(4)	11.913(4)
c (Å)	8.406(4)	8.404(4)
Volume (Å^3)	1193.83(2)	1192.82(2)
Overall isotropic displacement factor, Bov (Å^2)	1.95	0.225
χ^2	4.10	4.77
R_p (%)	2.52	1.35
R_{wp} (%)	3.26	1.76
R_{exp} (%)	1.61	0.81
μ_{Cu1} (μ_B)		−0.65
μ_{Cu2} (μ_B)		1.15

3.2.1. Muon spin rotation (μSR). Strong evidence of a conventional magnetic ordering is provided by μSR data taken in zero applied field. Indeed, as reported in figure 8, clear oscillations of the time evolution of the muon polarization (the 'asymmetry' of the muon decay [10]) are observed at 1.5 K. The signal combines several frequencies, as seen from the Fourier transform spectra of figure 9. This is a clear-cut signature of the existence of well-defined internal fields on several inequivalent muon stopping sites. These local fields cause a coherent precession of the muon spin components perpendicular to the local field direction, averaging to a 2/3 value of the total spin polarization for a powder sample. These well-defined oscillations are therefore characteristic of a magnetic long-range ordered state at low temperature. Also, the magnetic order arises from the bulk (nearly 100%) of the sample. The precession frequency ν_i is given by $\nu_i = \gamma_\mu/2\pi B_i$, where $\gamma_\mu/(2\pi) = 135.5$ MHz T^{-1} and B_i is the average magnitude of the local field at the ith muon site. In addition, the long-time asymmetry in our background-free experiment tends to the remaining non-oscillating 1/3 part of the total asymmetry which, in a static picture, accounts for the powder averaged fraction of the muon spin components that lie parallel to the local magnetic field. This 1/3 value is therefore typical of the absence of strong dynamical effects in this system. The existence of multiple sites is in tune with the structure since there are three inequivalent oxygen sites and, usually, in oxides, muons bind to an oxygen at a distance ∼1 Å. Note that there can be more magnetically inequivalent muon trapping sites than the number of inequivalent oxygen ions.

Typical spectra in a narrow temperature range around the magnetic transition are displayed in the bottom panel of figure 8. A slowly relaxing Gaussian asymmetry, originating solely from quasi-static nuclear dipolar fields, dominates the paramagnetic regime above the transition temperature (see the 16.58 K data). It is found to sharply replace the oscillating asymmetry in the selected narrow temperature range. This underlines the sharpness of the transition, which can be estimated to be at $T_N = 16.2(1)$ K from this

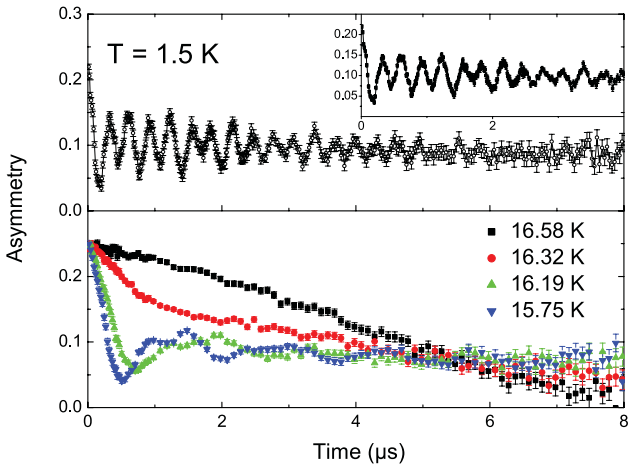

Figure 8. Top panel: zero field asymmetry at 1.5 K. In the expanded view of the inset, one can clearly identify the beats between several oscillating components. Bottom panel: evolution of the asymmetry around the transition from a slowly relaxing Gaussian shape at 16.58 K to an oscillating pattern already visible at 16.19 K.

plot, in fair agreement with that extracted from the zero field susceptibility and heat-capacity data. The temperature variation of the frequency of the oscillations can be followed up to the magnetic transition (figure 9) and scale with each other. This shows that once the order is established at T_N no further variation (even minute) of the magnetic structure occurs down to the lowest probed temperature.

After normalizing the frequencies (these track the order parameter) to their value at $T = 1.5$ K, we find that their temperature variation (in the temperature range above 10 K) obeys the following equation

$$\nu(T) = \nu(T = 0)[1 - (T/T_N)]^{\beta},$$

with $\beta = 0.26(2)$, and $T_N = 16.2(1)$. This exponent is less than that expected for three-dimensional models, $\beta = 0.367$ for the 3D Heisenberg model, but larger than the one expected for 2D XY models $\beta = 0.23$ [11].

3.2.2. Nuclear magnetic resonance (NMR). NMR measurements were carried out in the temperature range from 1.2 to 300 K in the phase coherent spectrometers at LPS (Orsay) attached to fixed-field and sweepable-field magnets. In these experiments, ^{45}Sc nuclei (nuclear spin $I = 7/2$ and gyromagnetic ratio $\gamma/2\pi = 10343.15$ kHz T^{-1}) were probed using the pulsed NMR technique. In the structure, ^{45}Sc nuclei are in an octahedral ScO_6 environment, with bond lengths as Sc–O1 $\sim$ 2.04 Å, Sc–O2 $\sim$ 2.11 Å, and Sc–O3 $\sim$ 2.18 Å, respectively. Since there is a slight deviation from perfect

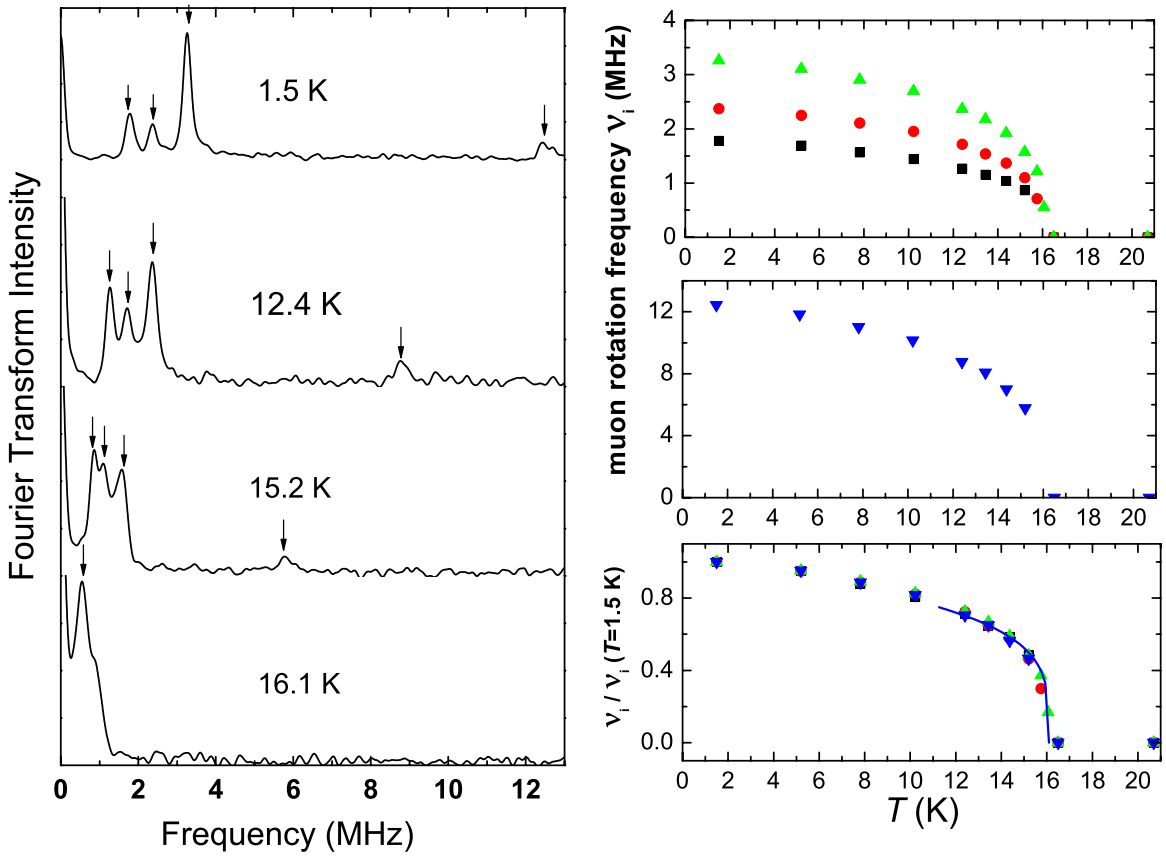

Figure 9. Left panel: Fourier transform of the oscillating asymmetry. Four muon sites are clearly evidenced. Right panel: temperature evolution of the frequencies corresponding to the four oscillating components of the muon asymmetry. In the lower graph, the variation of the normalized frequencies is plotted. The solid line is a fit to $1 - (T/T_N)^{\beta}$ (see text).

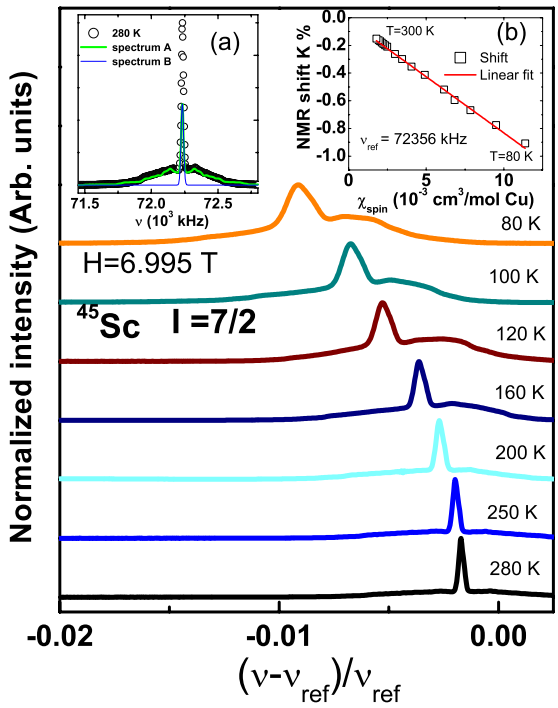

Figure 10. Normalized ^{45}Sc NMR spectra versus normalized frequency $(\nu - \nu_{\rm ref})/\nu_{\rm ref}$, where $\nu_{\rm ref} = (\gamma/2\pi)H$ is the reference frequency. Inset (a) shows the measured NMR spectrum as a function of frequency (ν), which can be simulated by combining a quadrupole split powder pattern (spectrum A) and a single line (spectrum B). The ratio of spectrum A and B is 1:1. (b) shows the NMR shift K versus the spin susceptibility along with a linear fit.

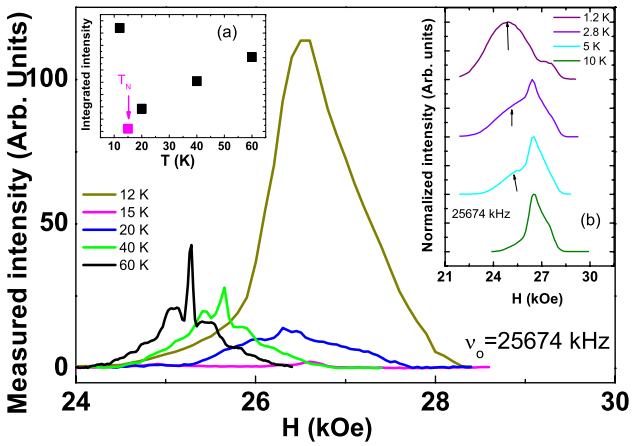

Figure 11. Measured ^{45}Sc NMR spin-echo intensity as a function of the applied magnetic field (swept-field experiment) at a fixed frequency $\nu_{\rm ref} = 25\,674$ kHz for various temperatures from 60 K to 12 K. The left inset shows the decrease of the NMR spectral intensity multiplied by temperature as one approaches the ordering temperature. The right inset shows the normalized NMR spectra for temperatures from 10 to 1.2 K.

octahedral symmetry, it may result in quadrupole-broadened NMR spectra.

3.2.2a. Spectra at high-T (above 80 K). Fourier transform spectra were obtained in a fixed field of ∼70 kOe in the temperature range from 80 to 300 K (see figure 10). Normalized intensities are plotted as a function of normalized frequency $(\frac{\nu_0-\nu_{\rm ref}}{\nu_0})$, where $\nu_{\rm ref} = \frac{\gamma}{2\pi}H = 72\,350.3$ kHz. In the case of single crystals, when quadrupole effects are present ($\nu_Q \neq 0$) and there is uniaxial symmetry ($\eta = 0$), the peak position gives K_z. Since ^{45}Sc nuclei in $Ba_3Cu_3Sc_4O_{12}$ are not in an environment of perfect octahedral symmetry, a quadrupole-broadened powder pattern is expected, with characteristic steps and singularities. Note that the satellite intensities (figure 10(a) inset) are smaller than those expected in a quadrupole powder pattern. This means that many sites have a nearly octahedral symmetry and a small ν_Q and the satellites come from a fraction of sites which deviate from the octahedral symmetry due to distortions. The observed spectrum at 280 K can be generated by a combination of a quadrupole powder pattern (spectrum A) with $\eta \sim 0.25$ and $\nu_Q \sim 400$ kHz and another one with a coincident central line (spectrum B) but $\nu_Q \sim 0$ (see inset of figure 10(a)).

The peak position changes with T and tracks the susceptibility ($N_A\mu_B K = A_{\rm hf}\chi_{\rm spin}$). The shift is calculated from the position of the maximum as from the formula $K_z = \frac{\nu_0^{\rm max}-\nu_{\rm ref}}{\nu_{\rm ref}}$. The obtained shifts as a function of spin susceptibility $\chi_{\rm spin}$ ($=\chi(T) - \chi_0$) are plotted in the inset of figure 10(b). The slope from a linear fit gives the total hyperfine coupling constant ($A_{\rm hf}$) between Sc and surrounding Cu atoms to be about −4.5 kOe. The chemical shift obtained from the intercept of the fit is nearly zero. In [5] the data were analyzed by plotting K as a function of T (rather than $\chi_{\rm spin}$). They observed a change of slope around 240 K and concluded the existence of a structural transition. In fact, we find the K versus T data to be Curie–Weiss-like and the 'change of slope' seen in [5] is not found by us (our temperature range is limited to 300 K, however). A progressive change in the shape of the spectrum takes place below 200 K and a large asymmetry is seen. This change with T may be related to structural distortions which create inequivalent sites.

3.2.2b. Spectra at low-T (below 80 K). The spectra broaden as T decreases due to a distribution of shifts which grows with decreasing temperature. Given the Curie–Weiss nature of the spin susceptibility above $T_{\rm N}$, a distribution of local environments for the ^{45}Sc nucleus will give this effect. In addition, the presence of an anisotropy of the susceptibility will as well contribute to an increased linewidth. Such broad spectra are measured more efficiently by sweeping the field at a fixed frequency rather than the Fourier transform technique used for $T \geq 80$ K. We measured the spectra at different frequencies 25 674 kHz and 61 674 kHz in the T-range from 1.2 to 80 K and these are plotted in figures 11 and 12, respectively. Figure 11 shows the measured intensity of NMR spectra as a function of T from 60 to 1.2 K in an applied field of about 25 kOe. Since the spectra are measured in low fields, the quadrupolar satellites are clearly seen at 60 K compared to the spectra measured in higher fields (see figure 12).

We find that the spectrum broadens as the ordering temperature is approached and the intensity is effectively lost near the ordering temperature at about $T = 15$ K (see left inset of figure 11). The critical slowing down of fluctuations near $T_{\rm N}$ causes a divergence of the relaxation rate and an

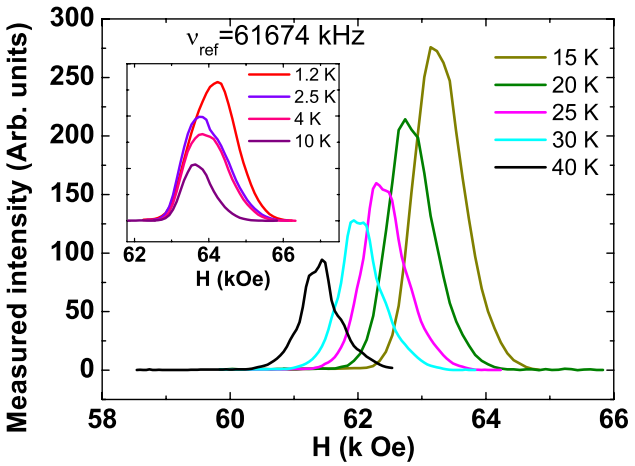

Figure 12. Measured spin-echo intensities of the ^{45}Sc NMR line as a function of the applied magnetic field (swept-field experiment) at a fixed frequency $\nu_{\rm ref} = 61\,674$ kHz for various temperatures from 40 to 15 K. Inset shows the NMR spectra for temperatures from 10 to 1.2 K.

effective disappearance of the signal. The spectrum reappears below the ordering temperature and the intensity increases rapidly with decreasing T . The increase of the linewidth with decreasing temperature (in the ordered state) indicates that ^{45}Sc experiences a distribution of static local fields (^{45}Sc is hyperfine coupled to inequivalent copper ions) which gives the large broadening. For better visual clarity, we have shown the normalized spectra in the temperature range from 10 K to 1.2 K separately in the inset of figure 11. The full width at half maximum at the lowest temperature measured (1.2 K) is about 3000 Oe from the spectrum at 25 674 kHz, while the total spread of the line is close to 5000 Oe. This is a measure of the field distribution seen at the ^{45}Sc site. From the crystal structure, it appears that ^{45}Sc is hyperfine coupled to three Cu ions, of which two are equivalent. The total hyperfine coupling was found to be −4.5 kOe. Therefore, the coupling per Cu is about -1.5 kOe/$\mu_{\rm B}$. Therefore with a 1 $\mu_{\rm B}$ magnetic moment localized at each Cu site, one would expect the total spread of the line to be around 4.5 kOe, consistent with our observation. In typical cases where antiferromagnetic ordering is observed, a single NMR line splits into two below the ordering temperature. This happens due to the internal field (at a magnetic site) either adding to or opposing the external magnetic field. However, one needs single crystals in order to observe the above-mentioned splitting. In the present case, we have polycrystalline samples (efforts to align these powders in an external field were not successful). Here, a rectangular line shape might be expected in the ordered state if the internal field at the ^{45}Sc sites is small compared to the applied field. Since there are inequivalent ^{45}Sc sites due to local distortions/defects, as already suggested by the room-temperature NMR spectrum in addition to a quadrupolar broadening, it results in a generic dome-shaped line shape.

In contrast to our μSR measurements, which were done in zero field, our NMR measurements have been done in various applied fields. Here, we are able to track the changes in the magnetic state due to an applied field. There are two main pieces of information that are obtained. (i) There is a decrease of the ordering temperature due to an applied field. In figure 12, the measured NMR spectra at a fixed frequency at 61 674 kHz (i.e. $H = 63$ kOe) in the T-range from 40 to 1.2 K are shown. In this field, the signal is retained down to 1.2 K (see also the inset of figure 12) due to the absence of ordering. (ii) There is possibly a change in the spin ordering as a function of temperature in the ordered state. As we see in the inset of figure 11, a broad feature (indicated by an arrow mark) is present at $T = 1.2$ K which vanishes progressively as the temperature is increased to $T = 10$ K. In the variation of bulk magnetization with H (see figure 3), there is a change in the slope of $M(H)$ at 23 kOe, which is smeared out in $M(H)$ isotherms at high temperature. So, the appearance of the broad feature in the NMR spectrum might be associated with the spin-flopped phase. In addition we have also plotted the spectra measured at $T = 1.2$ K at different frequencies $\nu_{\rm ref} = 18\,725$ kHz, $\nu_{\rm ref} = 25\,674$ kHz, $\nu_{\rm ref} = 29\,725$ kHz, and $\nu_{\rm ref} = 61\,674$ kHz in figures 13(a)–(d), respectively. The line width at 1.2 K is smallest for the highest frequency and/or field (where there is no ordering) and progressively increases at lower fields where the internal field distribution significantly affects the line shape. Particularly the line shapes of the spectra corresponding to $\nu_{\rm ref} = 18\,725$ kHz and $\nu_{\rm ref} = 25\,674$ kHz (which are in magnetic fields below 25 kOe) are different from the shape of the spectrum measured at $\nu_{\rm ref} = 29\,725$ kHz. This means that internal field below 25 kOe (where a spin-flop transition is observed) is different from the internal fields above 30 kOe. This change might be associated with the spin-flop transition observed in $M(H)$.

Thus, the information obtained from the local probe measurements mentioned above could be summarized as follows. Firstly, the existence of LRO at 16 K from the bulk of the sample is confirmed by μSR in zero field. The linear scaling of the NMR shift with the measured susceptibility ensures that the temperature-dependent part of the measured susceptibility is in fact the intrinsic spin susceptibility, confirming the sample to be free from magnetic defects/impurities. The loss in the intensity of the NMR signal well above the ordering temperature is indicative of the presence of short-range order or a large temperature regime of slow fluctuations. The field dependence of the ordering is also exhibited in the NMR measurements. In order to throw light on the various magnetic interactions which are important in BCSO, it is necessary to make an effort on the theoretical front. This is carried out in the next section, following which we arrive at a fuller understanding of BCSO.

3.3. Electronic structure calculations

Our analysis of the electronic structure of $Ba_3Cu_3Sc_4O_{12}$ are carried out in the framework of the tight-binding linearized muffin tin orbital (TB-LMTO) method in the atomic sphere approximation (ASA) within the local density approximation to the density functional theory [12]. The space filling in the ASA is achieved by inserting appropriate empty spheres and the TB-LMTO ASA band structure results are found to be in

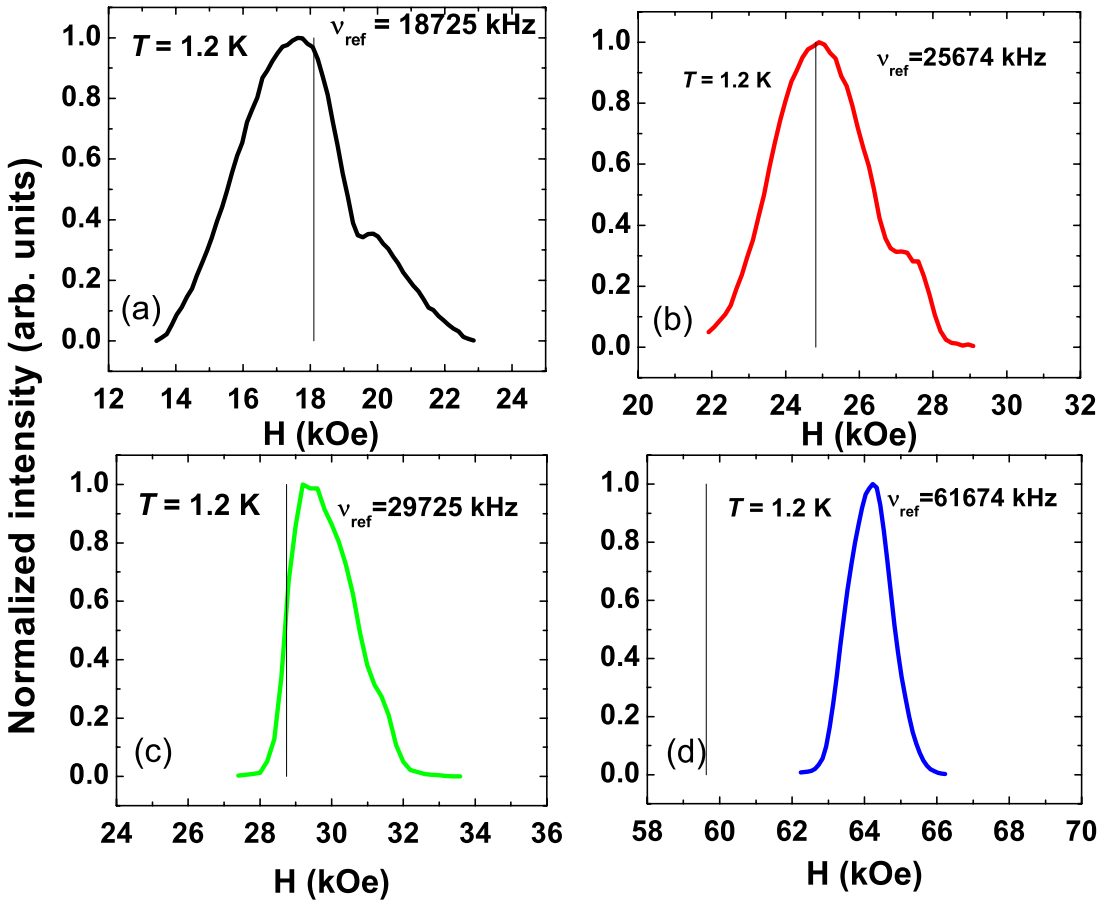

Figure 13. Variation of the ^{45}Sc NMR spectra at various radio frequencies at $T = 1.2$ K. The line is seen to get broader for lower frequencies (lower fields) due to the spin ordering related field distribution at ^{45}Sc site. The solid lines are the reference lines ($H_{\rm ref} = 2\pi\nu_{\rm ref}/\gamma$) for the corresponding reference frequencies.

good agreement with the full potential linearized augmented plane wave (FP-LAPW) calculations as implemented in the WIEN-2K code [15]. The basis set for the self-consistent electronic structure calculations for $Ba_3Cu_3Sc_4O_{12}$ in TB-LMTO ASA includes Ba (s, d, f), Cu (s, p, d), Sc (s, d) and O (s, p) and the rest are downfolded. A (16, 16, 16) k-mesh has been used for self-consistency. All the k-space integrations were performed using the tetrahedron method [14]. In order to extract a low-energy tight-binding (TB) model Hamiltonian and its various hoppings we have employed the Nth order muffin tin orbital (NMTO) based downfolding method [13]. For the calculations of the various exchange interactions we have performed total energy calculations in the framework of the GGA + U method for various ordered spin states. In order to extract the various exchange interactions, the relative energies of these ordered spin states determined from the GGA + U calculations are mapped onto the corresponding energies obtained from the total spin exchange energies of the Heisenberg spin Hamiltonian $H = -\sum_{i,j} J_{ij}\vec{S}_i \cdot \vec{S}_j$. The total energy calculations are carried out in the plane wave basis along with the projector augmented wave (PAW) method [16] as implemented in the Vienna *ab initio* Simulation Package (VASP) [17, 18]. The energy cut-off for the plane wave expansion of the PAW was taken to be 500 eV. The GGA + U calculations [19] are carried out for three different values of on-site d–d Coulomb interaction for Cu namely $U = 4$, 6, and 8 eV, while the on-site exchange parameter was fixed at 1 eV.

The all-orbital band structure along the various high symmetry points of the body centered tetragonal BZ obtained by TB-LMTO ASA calculations is displayed in figure 14. All the energies are measured with respect to the Fermi level $E_{\rm f}$. The characteristic feature of the band structure are half-filled six Cu d bands near the Fermi level. These bands arise from the six Cu atoms in the unit cell and are predominantly Cu $d_{x^2-y^2}$ character in a local frame of reference, where Cu is at the origin and the x and y axes point along the oxygens residing on the same square plaquette. This six-band complex is separated from the other completely filled non-Cu $d_{x^2-y^2}$ bands and O p bands by a gap of about 0.9 eV. The six-band complex hybridizes strongly with O1 and O3, forming a square plaquette for Cu1 and Cu2 respectively, and hardly with O2, which does not reside on these square plaquettes. This isolated Cu $d_{x^2-y^2}$ six-band complex is responsible for the low-energy physics of this material. While the system is metallic in LDA (see the DOS in the inset), inclusion of Coulomb correlations within LSDA + U makes the system insulating.

As the six-band manifold is well separated from the rest, so a tight-binding model with a single Cu $d_{x^2-y^2}$

Table 2. Hopping integrals (t_n) and exchange interactions (J) in meV.

Cu–Cu distance (Å)	Hopping (meV)	$J_i^{\mathrm{AFM}} = -4t_i^2/U_{\mathrm{eff}}$ (meV)	Exchange (meV) $U = 4$ eV	Exchange (meV) $U = 6$ eV	Exchange (meV) $U = 8$ eV
2.74	$t_1 = 16.3$	−0.27	14.58	12.40	13.88
3.53	$t_2 = 53.0$	−2.81	−8.22	−8.23	−6.93
4.19	$t_3 = 45.0$	−2.02	−5.58	−3.23	−2.74
4.88	$t_4 = 13.6$	−0.18	−10.5	−8.13	−2.53
6.88	$t_5 = 8.1$	−0.07	9.06	7.11	1.56
6.97	$t_6 = 5.4$	−0.03	−0.21	−0.09	−0.05
8.39	$t_{7a} = 8.0$	−0.06	0.32	0.38	1.03
8.39	$t_{7b} = 13.6$	−0.19	0.63	0.76	2.06
8.41	$t_8 = 19.0$	−0.36	1.70	−1.24	−3.89
9.15	$t_9 = 14.9$	−0.22	7.51	5.70	−0.03
9.40	$t_{10} = 18.0$	−0.32	−2.89	−2.21	−1.30
9.73	$t_{11} = 16.3$	−0.27	3.28	3.32	−0.22

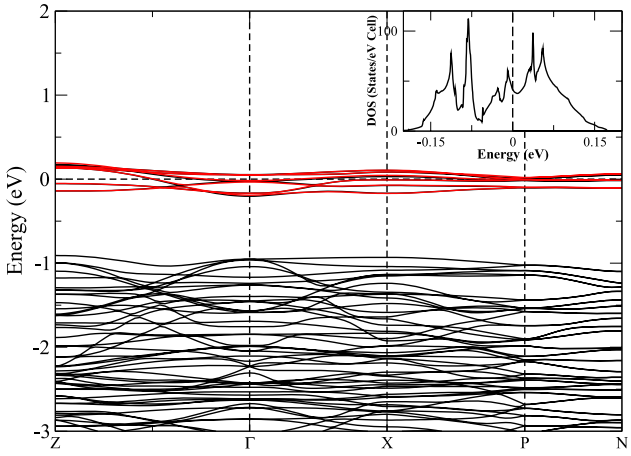

Figure 14. Downfolded band structure (shown as a red line) compared with the all-orbital LDA band structure. Inset shows the total density of states for $Ba_3Cu_3Sc_4O_{12}$.

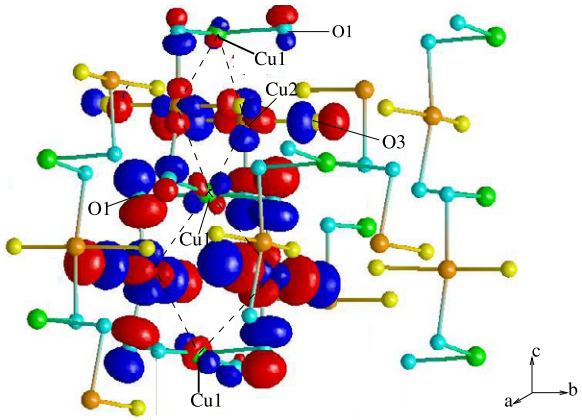

Figure 15. Effective Cu1 $d_{x^2-y^2}$ Wannier function plot for $Ba_3Cu_3Sc_4O_{12}$.

orbital per Cu site would be a good approximation to the full band structure close to the Fermi level. We have employed the NMTO downfolding method to construct a low-energy, few-band tight-binding model Hamiltonian for this system. The downfolding method consists of deriving a few-orbital effective Hamiltonian from the all-orbital LDA Hamiltonian by downfolding the inactive orbitals into the tails of the active orbitals kept in the basis chosen to describe the low-energy physics. This method results in renormalized effective interactions between the active orbitals (here Cu $d_{x^2-y^2}$) retained in the basis. In the present case the low-energy bands form an isolated set of bands and the constructed effective orbitals, the NMTO's are the Wannier functions corresponding to the low-energy bands. A real-space representation of the downfolded Hamiltonian via Fourier transform $\mathcal{H}(\mathbf{k}) \rightarrow \mathcal{H}(\mathbf{R})(\mathcal{H}(\mathbf{R}) = \sum_{\langle i,j \rangle} t_{ij}(c_j^\dagger c_i + c_i^\dagger c_j))$ yields the effective hopping parameters between the Cu ions. These hoppings will determine the dominant exchange paths and in turn will clarify the magnetic dimensionality of the system. The downfolded Cu $d_{x^2-y^2}$ bands are plotted in figure 14 and we note that the agreement with the full band structure is remarkable, thereby justifying our low-energy model Hamiltonian. Table 2 shows the various dominant effective hopping integrals between Cu ions at site i and j. These have been abbreviated as t_n, where n is a number indicating the path shown in figure 1. We gather from table 2, that the strongest hopping is t_2 between Cu2 and Cu2 in a particular diamond. As anticipated, Cu2 and Cu1 hopping in the diamond is weak due to its geometry, while unexpectedly Cu1–Cu1 coupling along the chain is quite strong. In order to obtain insights on the Cu1–Cu1 hopping t_3 we have plotted the Cu1 Wannier function in figure 15. We find from the figure that Cu1 $d_{x^2-y^2}$ strongly antibinds with the neighboring oxygens, which in turn antibind with Cu2 and again via oxygen to Cu1. It is interesting to note that the oxygen tails bend in order to strengthen the Cu–O bonding and, therefore, the Cu1–O–Cu2–O–Cu1 super-super-exchange path (SSE), resulting in a dominant t_3 interaction which is otherwise prohibited by symmetry. Table 2 also reveals that, in addition to the intra-chain hoppings, the inter-chain hoppings are quite dominant.

Guided by the various hopping strengths we have computed twelve exchange interactions for three different U values and the results of our calculations are presented in table 2. The antiferromagnetic contribution to the exchange using second-order perturbation is given by $J_i^{\mathrm{AFM}} = -\frac{4t_i^2}{U_{\mathrm{eff}}}$,

and is also listed in table 2; here t_i are various hoppings and U_{eff} is the effective Coulomb interaction, taken to be 4 eV in our calculations. From table 2, we gather that the dominant exchange interaction J_1 is ferromagnetic, while J_2, J_3, and J_4 are antiferromagnetic. As expected, antiferromagnetic J_2, J_3 and J_4 decrease with increasing U values. Further, inter-chain interactions J_5, J_9 and J_{11} are ferromagnetic. We note both intra-chain as well as inter-chain interactions are substantial, accounting for the magnetic long-range order seen for this system. The high-temperature behavior is dominated by the strong nearest-neighbor ferromagnetic exchange interaction J_1. This strong ferromagnetic exchange follows from the Anderson–Goodenough–Kanamori rules [20, 21] as the ∠Cu1–O1–Cu2 is 86.84° (close to 90°). At low temperature, further long-range interaction dominates, primarily mediated by oxygen via the super-super exchange and accounts for the antiferromagnetic behavior. An estimate of the asymptotic Curie–Weiss temperature θ obtained from the calculated exchange interactions within the mean field approximation [22] yields $\theta = 96$ K, 68 K and 55 K for $U = 4$, 6, 8 eV respectively, in good agreement with our experimental result (65 K).

4. Summary and conclusion

Our work on $Ba_3Cu_3Sc_4O_{12}$ was motivated by its crystal structure, which suggested the possibility of exotic magnetic behavior due to the apparent diamond-chain-like configuration of the magnetic Cu atoms. Whereas our detailed work has demonstrated the dominance of 3D magnetic interactions, there are several interesting features in the magnetism of this compound. The high-T magnetic susceptibility is Curie–Weiss-like, with a positive asymptotic Weiss temperature suggestive of *ferromagnetic* interactions. In contrast, the ordering is found to be antiferromagnetic, with the magnetic moments at the Cu1 and Cu2 sites aligned opposite to each other. This has to be seen in the light of our electronic structure calculations, which indicate comparable Cu1–Cu1 and Cu2–Cu2 interactions. A possible scenario that we have discussed in this paper is that the stronger Cu1–Cu2 ferromagnetic interaction (this exchange coupling is of the order of 160 K) drives the high-T Curie–Weiss behavior while the weaker Cu1–Cu1 and the Cu2–Cu2 antiferromagnetic exchanges (of the order of 50 K) drive the transition to AF order at low T. The sensitivity of the transition temperature to an applied magnetic field (a field of 70 kOe was sufficient to decrease the T_N from 16 K to zero, whereas one might have naively expected this to happen in a field of about 240 kOe) is, at first sight, somewhat puzzling and indicates the presence of competing interactions. This is also suggested by the heat-capacity measurements, where the observed entropy change due to the AF ordering is found to be smaller than the expected value of $R \ln 2$. Another interesting aspect is the change in slope in the low-temperature M versus H isotherms. This, coupled with the observed difference in the ^{45}Sc NMR line shapes at 1.2 K in various applied fields, points towards a change in the spin ordering with increasing applied field, at around 23 kOe. Our detailed electronic structure calculations have indicated the presence of a dominant ferromagnetic interaction and also several, somewhat weaker antiferromagnetic interactions. These calculations then enable us to qualitatively reconcile with our experimental data. We note that our μSR measurements were done in zero field, and the absence of any change in spin ordering seen there is not in contradiction to the above data. Yet another interesting feature has to do with the crystal structure. Since the ^{45}Sc nucleus has $I > 1/2$ its NMR spectrum should be a quadrupole powder pattern provided the site symmetry of the ^{45}Sc nucleus is lower than cubic. In $Ba_3Cu_3Sc_4O_{12}$, there are ScO_6 octahedra with only a slight deviation from the perfect octahedral environment (i.e., only a small crystalline electric field gradient efg at the center of each octahedron). Accordingly, the room-temperature NMR spectrum of ^{45}Sc in $Ba_3Cu_3Sc_4O_{12}$ exhibits weak satellite intensities, suggesting that many of the sites feel a negligible electric field gradient while the remaining give rise to a quadrupole-broadened powder pattern, presumably due to structural distortions around them.

To conclude, our extensive measurements, coupled with *ab initio* electronic structure calculations (where we have determined the relative strengths and the signs of the exchange interactions between various copper ions and also the asymptotic Weiss temperature θ), have helped in developing a comprehensive understanding of the magnetic properties of $Ba_3Cu_3Sc_4O_{12}$. In particular, we find that our work shows that the system is complex, therefore a naive assessment of the crystal structure/atomic arrangement to arrive at a conclusion regarding the magnetic dimensionality can be misleading and a theoretical determination of the various important magnetic couplings is essential for a complete picture.

Acknowledgments

We thank the Indo-French Center for the Promotion of Advanced Research and ARCUS Ile de France-Inde. SR and VS are grateful to Professor A K Raychaudhuri and DST, India for travel funding. JC acknowledges CSIR, India for a research fellowship. We thank A Amato for technical support with the GPS instrument at the Swiss Muon Source, Paul Scherrer Institute, Villigen, Switzerland where the μSR work was performed.

References

[1] Kikuchi H, Fujii Y, Chiba M, Mitsudo S, Idehara T, Tonegawa T, Okamoto K, Sakai T, Kuwai T and Ohta H 2005 *Phys. Rev. Lett.* **94** 227201
Gu Bo and Su G 2006 *Phys. Rev. Lett.* **97** 089701
Kikuchi H *et al* 2006 *Phys. Rev. Lett.* **97** 089702
[2] Rule K C *et al* 2008 *Phys. Rev. Lett.* **100** 117202
[3] Jeschke H *et al* 2011 *Phys. Rev. Lett.* **106** 217201
[4] Gregory D H, Mawdsley P R, Barker S J, Daniell W and Weston D P 2001 *J. Mater. Chem.* **11** 806
[5] Gippius A A *et al* 1989 *Sov. Phys.—JETP* **68** 1226
[6] Rodriguez-Carvajal J 1993 *Physica* B **192** 55
[7] Siruguri V, Babu P D, Gupta M, Pimpale A V and Goyal P S 2008 *Pramana* **71** 1197

[8] Selwood P W 1956 *Magnetochemistry* (New York: Interscience)
[9] Kittel C 1996 *Introduction to Solid State Physics* (Singapore: Wiley)
[10] See, for example, Lee S L, Kilcoyne S H and Cywinskin R 1999 Muon Science *SUSP Proc.*
[11] Bramwell S T and Holdsworth P C W 1993 *J. Phys.: Condens. Matter* **5** L53
[12] Andersen O K and Jepsen O 1984 *Phys. Rev. Lett.* **53** 2571
[13] Andersen O K and Saha Dasgupta T 2000 *Phys. Rev.* B **62** R16219
[14] Blöchl P E *et al* 1994 *Phys. Rev.* B **49** 223
[15] Blaha P, Schwartz K, Madsen G K H, Kvasnicka D and Luitz J 2001 *WIEN2K, An Augmented Plane Wave + Local Orbitals Program for Calculating Crystal Properties* ed K Schwarz (Austria: Technische Universität Wien)
[16] Blöchl P E 1994 *Phys. Rev.* B **50** 17953
[17] Kresse G and Hafner J 1993 *Phys. Rev.* B **47** 558
[18] Kresse G and Furthmüller J 1996 *Phys. Rev.* B **54** 11169
[19] Dudarev S L, Botton G A, Savrasov S Y, Humphreys C J and Sutton A P 1998 *Phys. Rev.* B **57** 1505
[20] Goodenough J B 1963 *Magnetism and the Chemical Bond* (New York: Interscience)
[21] Kanamori J 1959 *J. Phys. Chem. Solids* **10** 87
[22] Koo H J and Whangbo M H 2008 *Inorg. Chem.* **47** 4779